

# Inverse physics-informed neural networks for digital twin-based bearing fault diagnosis under imbalanced samples

Yi Qin<sup>a</sup>, Hongyu Liu<sup>a</sup>, Yi Wang<sup>a</sup>, Yongfang Mao<sup>b,\*</sup>

<sup>a</sup> State Key Laboratory of Mechanical Transmission for Advanced equipment, Chongqing University, Chongqing 400044, PR China

<sup>b</sup> School of Automation, Chongqing University, Chongqing 400044, PR China



## ARTICLE INFO

### Keywords:

Digital twin  
Physics-informed neural network  
Bearing dynamic model  
Fault diagnosis  
Sample imbalance

## ABSTRACT

In actual engineering, insufficient bearing samples for each fault category presents a substantial obstacle to the intelligent fault diagnosis of rolling bearings. To address sample imbalance, this work explores a novel bearing fault data-generation approach based on digital twin technique. First, an inverse physics-informed neural network (PINN) is built to recognize dynamic model parameters by embedding a bearing dynamic model into a neural network. In this network, a boundary loss is designed to quickly determine the approximate ranges of parameters that can accelerate network convergence, and a true value loss is constructed for the assessment of spectral discrepancy between simulated and actual data. Then, using an inverse PINN, a bearing fault dynamic model, and real vibration data, we propose a digital twin-based fault data-generation method for producing high-quality bearing fault samples under multiple working conditions and fault modes. Finally, the developed approach is applied to generate bearing fault vibration samples under a specific working condition. The samples are used for training the diagnostic network, thus solving the issue of sample imbalance. The comparison results of several experiments suggest that the developed data-generation method effectively improves the precision of cross-working-condition bearing fault diagnosis and surpasses multiple state-of-the-art methods.

## 1. Introduction

Rolling bearings are the basic components of important equipment, such as precision machine tools, aircraft, and high-speed trains, and their health states often influence the service behavior of the whole equipment. As critical equipment usually operates in the varied speed and heavy load, rolling bearings are susceptible to failure. Approximately one-third of equipment accidents are caused by bearing faults. Therefore, the real-time monitoring and fault detection of rolling bearings assure the reliability and safety of equipment.

Proposed methods for bearing fault diagnosis can be broadly categorized into signal processing-based approaches [1] and artificial intelligence-based techniques [2]. Deep learning methods, including convolutional neural networks (CNNs) [3], deep neural networks [4], and federated learning [5], play a dominant role in intelligent bearing fault diagnosis. However, these deep learning methods typically demand a substantial number of fault samples. In many engineering applications, normal bearing vibration signal samples are abundant, but the availability of fault vibration signal samples is limited. Moreover, some faults may have considerably fewer samples than others. Consequently, a

bearing dataset exhibits sample imbalance, which can significantly impact the efficacy of fault diagnosis. The scarcity of fault samples and the imbalance of datasets may inhibit fault diagnosis models from identifying some fault types. To address these issues, Zhao et al. [6] proposed an approach based on wavelet packet and a CNN for imbalanced machine fault diagnosis, and Xu et al. [7] studied a cost-sensitive learning method capable of multidomain feature extraction and selection, which effectively reduced false negatives and average cost. In addition, Li et al. [8] introduced continual learning to improve the effect of fault diagnosis when training data types are scarce. Another available approach is to add related fault samples.

Data generation based on actual signals is a feasible sample-augmentation technique. Wang et al. [9] built an adaptive and efficient subpixel network called DAESPN for fault sample augmentation and intelligent fault diagnosis under fluctuating speed conditions. An et al. [10] developed an actively imaginative data augmentation model to enhance bearing fault diagnosis. Pei et al. [11] designed an improved Wasserstein autoencoder based on meta-learning to augment rolling bearing data and enhance bearing fault diagnosis. However, these data-driven approaches often require a large number of actual samples

\* Corresponding authors.

E-mail address: [yfm@cqu.edu.cn](mailto:yfm@cqu.edu.cn) (Y. Mao).

for the training of generative models, and the generated samples are often similar to training samples, limiting diversity and hindering increase in fault diagnosis accuracy.

An alternative approach is the utilization of a fault dynamic model for generating fault samples. Shao et al. [12] developed a rotor-bearing system dynamics model, which produced bearing vibration signals with different health states; these signals were subsequently employed for the fault diagnosis of real bearings with a generative adversarial network (GAN). Qin et al. proposed a fault dynamics model using time-varying excitation to generate fault samples [13]. Similarly, Liu et al. et al. [14] established a phenomenological bearing vibration model for the production of fault samples, which were also utilized for GAN-based bearing fault diagnosis. Liu et al. [15] proposed a personalized fault diagnosis method to activate smart sensor networks through finite element simulation; the method improved the effectiveness of fault diagnosis when fault samples were missing. However, a data-generation method based on a dynamic model needs to determine the key parameters of a fault-bearing dynamic model, such as stiffness and damping ratio. These parameters are generally set by experience. The difference between the estimated and actual parameters leads to a discrepancy between simulation and measurement data, impacting the effect of simulation data on the training of diagnostic model. The digital twin model only requires few actual signals to generate fault samples, thus conserving experimental materials and time.

Combining data-driven and model-based methods, sample augmentation techniques based on digital twins have attracted considerable interest. They only require few actual signals to generate fault samples, thus reducing the experimental cost. Some approaches for augmenting bearing vibration data have been proposed. Piltan et al. [16] built a bearing digital twin framework combining a mechanism model with an adaptive observer to accurately detect bearing crack size. To expound bearing vibration response during degradation, Qin et al. [17] established a bearing digital twin model in the full life cycle. Notably, a novel mapping network based on cycle GAN (CycleGAN) [18] minimize the discrepancy between simulation and actual signals. Unfortunately, these studies have focused on mapping from virtual simulation data to physically real data to generate high-quality samples and ignored mapping from the physical space to the virtual space, that is, the parameters of the dynamic models were not tuned using measured signal. In addition, the dynamic models were not fully integrated into neural networks.

To combine physical models with neural networks, various physics-informed neural networks (PINNs) have been proposed, some of which were successfully applied to fault prognosis and rolling bearing diagnosis. For example, Chen et al. [19] proposed a physical information-degeneration consistency recurrent neural network for predicting machine RULs and integrated the degradation capabilities of machine components into a neural network. Yucesan et al. [20] built a physical information-based PINN for modeling the fatigue of main bearing in wind turbines. However, these methods mainly utilized physical information for RUL prediction rather than solving physical models. Some PINNs for solving various physical models have been proposed. For instance, Ling et al. [21] predicted turbulence by using a PINN, and Mao et al. [22] modeled high-speed aerodynamic flows with PINN. Unfortunately, current PINNs cannot compute the vibration response of two-degree-of-freedom (2-DOF) bearing dynamic models because two differential equations are coupled to each other. Therefore, PINN should be improved to dynamically model faulty rolling bearing.

Stiffness and damping ratio are two important parameters in the bearing dynamics model, and they are generally set by experience, which often leads to a large discrepancy between simulated and measured signals. To address this gap, an inverse PINN for rolling bearing is proposed. In contrast to the traditional PINN, the 2-DOF differential equations of rolling bearing rather than loss functions are used for the direct calculation of a vibration response, and network loss is regarded as the spectral discrepancy between simulated and acquired real signals for the prevention of the coupling effect between two

dynamic differential equations along the X and Y directions. Meanwhile, the optimization object of the inverse PINN are the dynamic parameters of bearing rather than the vibration response, and thus it can precisely identify the parameters of a bearing dynamic model. Using the inverse PINN and bearing dynamic model, we develop a novel fault data-generation method for producing high-precision bearing vibration signals under various working conditions. Finally, the generated data are successfully applied to the cross-working-condition bearing fault diagnosis in the presence of imbalanced samples.

The contributions of this research are as follows:

- 1) To identify the parameters of dynamic model, we propose an inverse PINN, where a bearing dynamic model is integrated into a neural network. In this network, boundary loss is designed to quickly determine the approximate ranges of parameters, which can accelerate network convergence, and a true value loss is constructed for the assessment of the spectral difference between simulated and real data. With the proposed inverse PINN, the dynamic parameters of bearing can be accurately identified.
- 2) Using the inverse PINN, the bearing fault dynamic model, and the acquired vibration signals, we propose a novel data-generation approach based on digital twins to generate high-quality fault samples under multiple working conditions. From a small number of bearing samples acquired under a single working condition, this method can generate high-quality bearing fault vibration samples under different working conditions. Evidently, the proposed method achieves the digital twin of fault rolling bearings.
- 3) For cross-working-condition fault diagnosis with the imbalanced bearing vibration samples, the proposed approach is used to generate bearing fault vibration samples under a specific working condition. Then, the samples are used for the training of the diagnostic network. The experimental result indicate that the proposed approach can improve the precision of cross-working-condition bearing fault diagnosis comparing with various state-of-the-art (SOTA) data-generation and imbalanced fault diagnosis methods.

The rest of this article is structured as follows. The preliminary knowledge of PINN and digital twin is briefly presented in Section 2. In Section 3, the inverse PINN is established, and the high-precision fault data-generation method based on digital twins is developed. In Section 4, the fault samples of two types of rolling bearings are generated by the proposed method, and they are applied to the cross-working-condition fault diagnosis of rolling bearings. The comparison results validate the superiority of the proposed method over other methods. Section 5 provides the conclusion.

## 2. Preliminaries

### 2.1. PINN

PINNs can incorporate empirical data and abstract mathematical operators [23], such as partial differential equations (PDEs). Once physical principles or constraints are embedded into a PINN, the network exhibits enhanced interpretability and anti-interference capability. In general, the loss of a typical PINN is defined as

$$\mathcal{L} = w_{\text{data}} \mathcal{L}_{\text{data}} + w_{\text{PDE}} \mathcal{L}_{\text{PDE}} + w_b \mathcal{L}_b, \quad (1)$$

where  $\mathcal{L}_{\text{data}}$  represents the gap between the output data and the real data,  $\mathcal{L}_b$  represents the initial value and boundary loss, and  $\mathcal{L}_{\text{PDE}}$  is determined by the differential equation;  $w_{\text{data}}$ ,  $w_{\text{PDE}}$ , and  $w_b$  are the weights for balancing the effects of the interactions among the three losses, which can be user-defined or automatically adjusted. The parameters of PINN are optimized by minimizing loss through various gradient-based optimizers (e.g., Adam and L-BFGS). However, the traditional PINN is mainly applied to solve a single PDE.

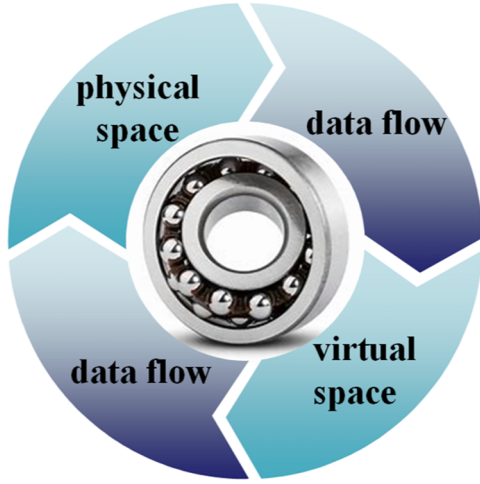


**Fig. 1.** Schematic diagram of digital twin framework.

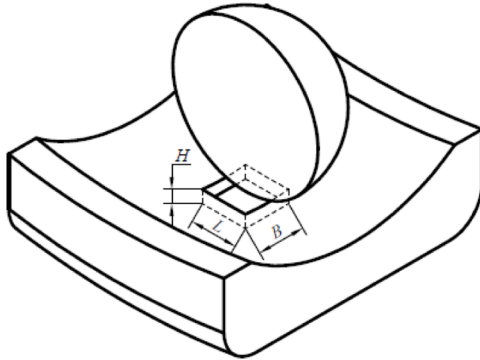


**Fig. 2.** Shape of the simplified fault.

## 2.2. Digital twin

As a novel approach for equipment operation and maintenance, the digital twin technology originates from a lecture delivered by Professor Grieves at the University of Michigan in 2003 [24]. In this lecture, the digital twin model was defined, which contain three fundamental components: virtual space, physical space, and interconnectedness of data flows. In 2012, NASA [25] regarded digital twin as a simulated process that integrate several physical domains, scales, and probabilities. This innovative approach has proven successful in design, manufacturing, and operation and maintenance of various pieces of equipment. Deon et al. [26] established the digital twin model of thermal power plant generator sets for predictive maintenance. As shown in Fig. 1, a digital twin framework is mainly composed of physical space, virtual space, and data flow or mapping relationship between them. The physical space denotes the analyzed system or component; the virtual space is the established analysis model, such as a finite element model or lumped-parameter dynamic model.; and the data flow or mapping is used to bridge the relationship between the physical and virtual space. To address sample imbalance in bearing fault diagnosis, we utilize the digital twin technology to generate bearing fault samples.

## 3. Proposed methodology for bearing fault vibration data generation

### 3.1. Bearing fault dynamics model

A bearing fault dynamics model is first built. The complexity of the model is reduced by simplifying the bearing fault on the outer race into a

cube (Fig. 2). The length, width, and height of a cube are denoted by  $L$ ,  $B$ , and  $H$ , respectively. According to the fault and rolling bearing parameter, the maximal displacement excitation  $\Delta H$  caused by the fault is calculated by

$$\Delta H = \begin{cases} \Delta H' & \Delta H' < H \\ H & \Delta H' \geq H \end{cases}, \quad (2)$$

$$\Delta H' = 0.5D - ((0.5D)^2 - (0.5\min(L, B))^2)^{0.5}, \quad (3)$$

where  $D$  represents the diameter of the roller and  $\Delta H'$  is the theoretical maximum of displacement excitation.

Considering the half sine excitation, we can define the displacement excitation function as follows [27]:

$$\begin{cases} h_j = \Delta H \sin\left(\frac{\pi}{\varphi_2 - \varphi_1} (\text{mod}(\theta_j, 2\pi) - \varphi_1)\right), & \varphi_1 \leq \text{mod}(\theta_j, 2\pi) \leq \varphi_2, \\ h_j = 0, & \text{otherwise} \end{cases}, \quad (4)$$

where  $\varphi_1$  represents the angle between the roller and X-axis when entering the fault area,  $\varphi_2$  represents the angle between the roller and X-axis when exiting the fault area, and  $\theta_j$  represents the position of the  $j$ th roller.

The normal deformation of the contact between the race and roller includes the influence of the bearing fault displacement excitation function. The contact deformation expression is

$$d_j = \delta_x \cos \theta_j + \delta_y \sin \theta_j - \varepsilon - h_j, \quad (5)$$

where  $\delta_x$  and  $\delta_y$  represent the displacement of the rolling bearing in the X and Y directions, respectively, and  $\varepsilon$  denotes the bearing tolerance.

The 2-DOF dynamic equation of the faulty bearing is formulated as

$$\begin{cases} m\ddot{\delta}_x + c\dot{\delta}_x + K \sum_{j=1}^{N_b} \mu_j (\delta_x \cos \theta_j + \delta_y \sin \theta_j - \varepsilon - h_j)^{1.5} \cos \theta_j = W_x \\ m\ddot{\delta}_y + c\dot{\delta}_y + K \sum_{j=1}^{N_b} \mu_j (\delta_x \cos \theta_j + \delta_y \sin \theta_j - \varepsilon - h_j)^{1.5} \sin \theta_j = W_y \end{cases}, \quad (6)$$

where  $m$  denotes the equivalent bearing mass;  $K$  represents the force-deformation coefficient (i.e., stiffness);  $c$  is equivalent damping ratio;  $\mu_j$  denotes the judgment coefficient of the  $j$ th roller in the contact area and is given by

$$\mu_j = \begin{cases} 1 & \delta_j \geq 0 \\ 0 & \delta_j < 0 \end{cases}. \quad (7)$$

The stiffness  $K$  and damping ratio  $c$  are the two key parameters in the bearing fault dynamic model and greatly influence the quality of simulated vibration response. However, they are usually set through practical experience. In the following section, we will discuss how to precisely recognize  $K$  and  $c$  through the measured bearing fault vibration signal.

### 3.2. Inverse pinn

In this section, the proposed inverse PINN will be elaborated.

**1) Principle of the inverse PINN:** Different from current PINNs, the optimization objective of the proposed inverse PINN is obtaining two dynamic parameters rather than a bearing vibration response. The structure diagram of the inverse PINN is shown in Fig. 3. The input of the inverse PINN is the measured fault vibration signal of the rolling bearing from the actual physical space, and its outputs are dynamic parameters. During network training, the dynamic parameters are updated. With the updated dynamic parameters and the known structure parameters of the rolling bearing, such as number of rollers, roller diameter, fault location, and initial angular position, the nonlinear bearing fault dynamic

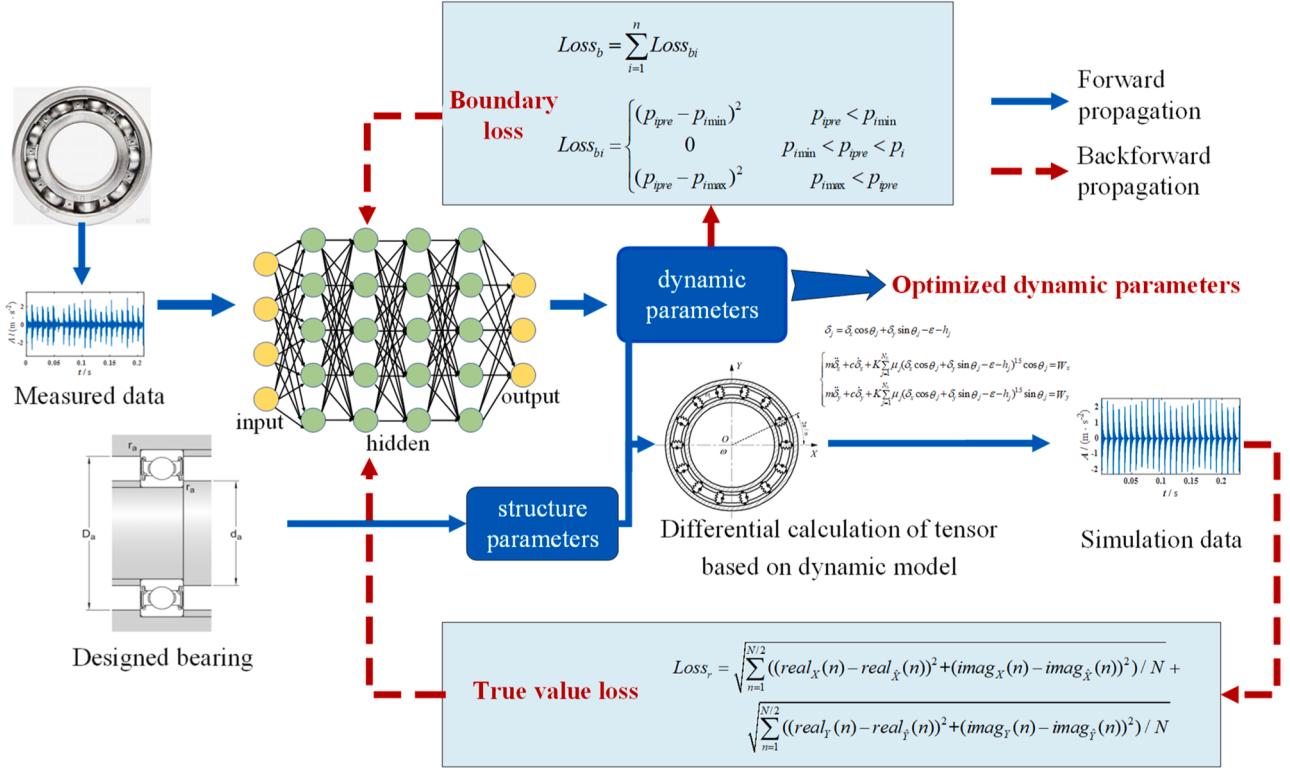


Fig. 3. Inverse PINN structure.

**Table 1**  
Structure of the inverse PINN.

Type of layer	Core size/stride	Number of cores	Output size
Conv 1	4 × 4/1	32	(1, 37, 32)
Conv 2	4 × 4/1	64	(1, 34, 64)
Conv 3	4 × 4/1	128	(1, 31, 128)
Conv 4	4 × 4/1	256	(1, 28, 256)
Conv 5	4 × 4/1	512	(1, 25, 512)
Dense	/	/	2

equation is solved using the Runge–Kutta method along with tensor calculations, and the vibration responses of faulty bearing along the X and Y directions are obtained. Then, the difference between the FFTs of measured and simulated signals is computed as the loss. Moreover, the boundary loss in two dynamic parameters is designed for network training.

Given that the difference between the stiffness  $K$  and the damping ratio  $c$  is an order of magnitude high,  $K$  is not directly output by the neural network and is obtained by multiplying the network output value by seven orders of magnitude. This approach can ensure that the two parameters of a network output are in a similar order of magnitude as much as possible and facilitate the convergence of the proposed network. The goal of the inverse PINN is different from that of the original PINN, and former has a simpler structure than the latter. The structure of the inverse PINN is shown in Table 1.

**2) Loss function of the inverse PINN:** The loss function of the inverse PINN consists of two parts. The first part is boundary loss, which contains the boundary conditions of all unknown parameters. The boundary loss in the traditional PINN is mainly used to constrain the response value or physical quantity at a certain time or space point. For example, in the PINN based on fluid mechanics, the fluid velocity at a certain position is zero or a certain value, and this information can be utilized for formulating the boundary loss. However, in the inverse PINN, the target value is no longer a specific response, but the unknown

physical parameters. The approximate value ranges of these parameters are used as boundary conditions. As the dynamic parameters are updated within the specific ranges, the network training can be accelerated. The boundary loss  $Loss_b$  is expressed as

$$Loss_b = \sum_{i=1}^n Loss_{bi}, \quad (8)$$

$$Loss_{bi} = \begin{cases} (p_{ipre} - p_{imin})^2 & p_{ipre} < p_{imin} \\ 0 & p_{imin} < p_{ipre} < p_{ipmax} \\ (p_{ipre} - p_{ipmax})^2 & p_{ipmax} < p_{ipre} \end{cases} \quad (9)$$

where  $p_{ipre}$  denotes the  $j$ th parameter output by the network model;  $p_{imin}$  and  $p_{ipmax}$  are the lower and upper limits of the parameter, respectively; and  $n$  is the number of parameters. In this work, two dynamic parameters are considered: bearing stiffness  $K$  and damping ratio  $c$ . The specific upper and lower limits are set according to the value ranges of two parameters. The approximate range of parameter values can be determined according to the empirical knowledge about the target bearing. For example, the damping ratio of a bearing usually ranges from 10 to 1000, and stiffness usually ranges from  $10^8$  to  $10^{10}$ .

The second part of the loss function is the discrepancy between the simulation vibration and measured signals. The influence of noises in the measured signal samples is suppressed by calculating the loss function of this part in the frequency domain. Interferences by phase difference and other factors are prevented by converting the time-domain signals into frequency-domain signals. Moreover, dynamic parameters, including stiffness and damping ratio, have a more considerable influence on frequency spectrum than a time-domain signal. Therefore, a loss function based on frequency-domain signals ensures the accurate and quick optimization of these parameters. The root mean square error (RMSE) between the frequency-domain transformation results of measured and simulated vibration signals are obtained as losses and called true  $Loss_r$  values. This loss is defined as

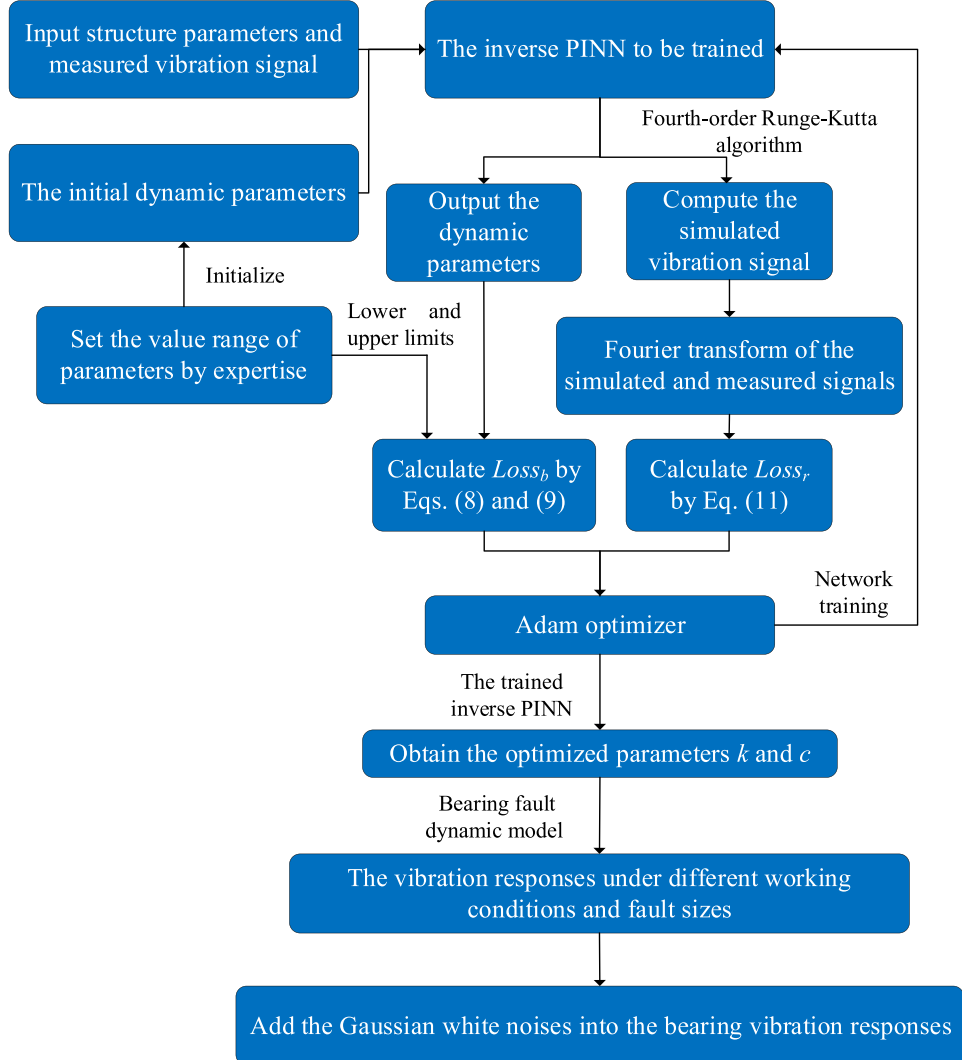


**Fig. 4.** Specific steps of the proposed digital twin-based fault data-generation method.

$$Loss_r = \sqrt{\sum_{n=1}^{N/2} ((real_X(n) - real_{\hat{X}}(n))^2 + (imag_X(n) - imag_{\hat{X}}(n))^2)/N + \sum_{n=1}^{N/2} ((real_Y(n) - real_{\hat{Y}}(n))^2 + (imag_Y(n) - imag_{\hat{Y}}(n))^2)/N}, \quad (10)$$

where  $X$  and  $Y$  are the Fourier transform of measured vibration signals along the X and Y directions;  $\hat{X}$  and  $\hat{Y}$  are the Fourier transform of the simulated vibration signals corresponding to the dynamic parameters updated by the inverse PINN;  $real(\bullet)$  and  $imag(\bullet)$  denote the real and imaginary parts of the data, respectively. The true value loss effectively reduces the spectral difference between the simulated and measured signals. Using this loss to train the inverse PINN, the dynamic parameters closer to the real situation can be obtained. Then, these dynamic parameters are introduced into the bearing fault dynamic model, thereby improving the similarity between the simulated and measured signals.

In summary, the loss of the proposed inverse PINN is formulated as

$$Loss = Loss_b + Loss_r. \quad (11)$$

### 3.3. Bearing fault data generation

With the proposed inverse PINN, a fault data-generation method based on digital twin is proposed, and its specific steps are given below.

**Step 1:** Input the structure parameters of rolling bearing, and feed the measured vibration signal acquired under a working condition into the inverse PINN. Set the value ranges of two dynamic parameters by expertise, then initialize the two dynamic parameters within the two ranges respectively.

**Step 2:** According to the structure parameters, working condition, and dynamic parameters, solve the 2-DOF dynamic equation of the faulty bearing by using the Runge-Kutta algorithm in conjunction with tensor calculations. Then, obtain the simulated vibration signal.

**Step 3:** Compute the Fourier transform of the simulated vibration and measured signals. Compute the output dynamic parameters by the inverse PINN.

**Step 4:** Compute the true value loss  $Loss_r$  through Eq. (11). Then, compute the boundary loss  $Loss_b$  with Eqs. (8) and (9).

**Step 5:** Using the obtained loss, train the inverse PINN with the Adam optimizer. Tune the network parameters through the loss.

**Step 6:** Repeat Steps 2 to 5 until the inverse PINN converges. After completing the network training, accurately identify the two dynamic parameters  $k$  and  $c$ .

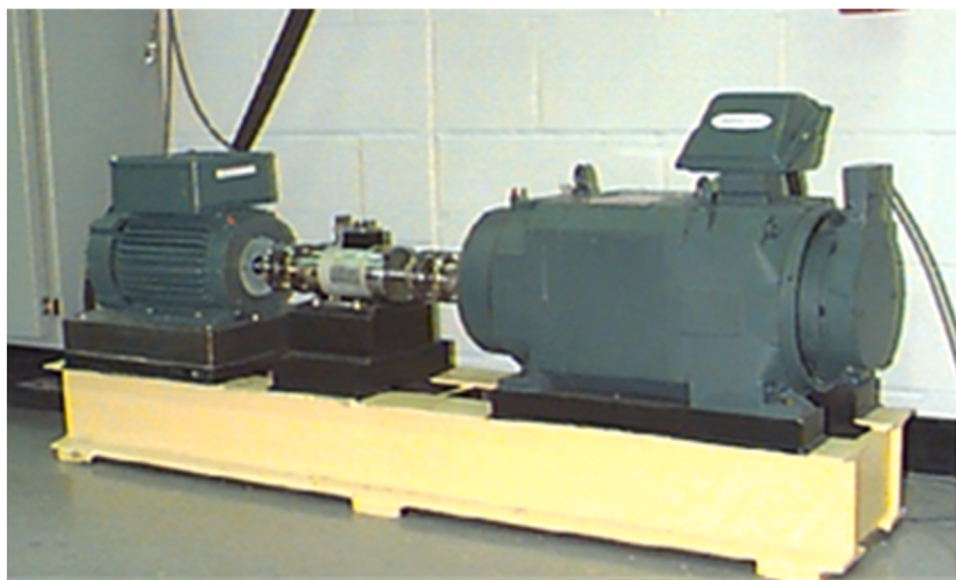


**Fig. 5.** Faulty rolling bearing test rig used by CWRU.

**Table 2**  
Bearing parameters from CWRU.

Name	Value
Number of balls ( $n$ )	9
Roller diameter ( $d_r$ /mm)	7.94
Pitch diameter ( $d_m$ /mm)	39
Inner race diameter ( $d_i$ /mm)	31.06
Outer race diameter ( $d_o$ /mm)	46.94
Initial contact angle ( $\alpha$ /°)	0

**Step 7:** Submitting the obtained dynamic parameters into the bearing fault dynamic model, compute the simulated vibration signals with various working conditions and fault modes (including fault sizes).

**Step 8:** Add Gaussian white noises to the bearing vibration responses to improve the diversity of the generated data.

The above procedure is illustrated in Fig. 4. Add the simulated bearing fault samples to the training set to resolve sample imbalance and improve the precision of an imbalanced fault diagnosis.

#### 4. Experiment and analysis

##### 4.1. Experimental description

The proposed approach will be validated by two experiments. The first experiment is based on the bearing fault test from the Case Western Reserve University (CWRU). The test rig is illustrated in Fig. 5, which mainly consists of a driving motor (left), a torque sensor (middle), and a torque motor (right). The two test SKF bearings (6205-2RS) are located at the bearings. The vibration signal from the faulty rolling bearing with a fault diameter of 0.54 mm (i.e.,  $L = B = H = 0.54$  mm) at the driving end is used. During the experiment, the motor's rotation speed is 1750 rpm, and the signals are sampled at a frequency of 12 kHz. The structure parameters are listed in Table 2.

The second experiment is based on the bearing fault test from Xi'an Jiaotong University (XJTU) [28]. The bearing test rig is illustrated in Fig. 6, which is mainly used for bearing degradation tests. Two accelerometers manufactured by PCB Company are employed for the detection of the bearing acceleration signals along the X and Y directions at a sampling frequency of 25.6 kHz. The bearing type is LDK UER204, and

its structural parameters are illustrated in Table 3.

##### 4.2. Training details

The hardware for computation mainly comprises Intel e5-2643 CPU, 16 GB memory, and 3080 GPU. Python 3.8 and Tensorflow2 and NumPy packages are used to train the neural networks. Each training sample in the training dataset contains 1600 points. The proposed inverse PINN is trained for 1000 epochs, where the momentum term is set at 0.5. An Adam optimizer is used, and the learning rate for training the discriminator is 0.0001.

##### 4.3. Experimental result analysis

In the CWRU and XJTU experiments, the dynamic parameters (Table 4) of the faulty rolling bearings are estimated by the inverse PINN. Meanwhile, empirical parameters set by other works [17,27] are also listed in Table 4. A large difference between the two types of dynamic parameters is observed. Different dynamic parameters lead to different vibration responses. In the CWRU experiment, the vibration signals are calculated using the two types of dynamic parameters. The simulated and measured signals are concurrently shown in Fig. 7. In the time-domain waveforms, determining whether the optimized parameters are better than the empirical parameters or vice versa is difficult.

The dynamic parameters  $k$  and  $c$  do not affect the rotational frequency and the fault characteristic frequency, but they influence other frequency components, such as natural frequency. To clarify the influence of dynamic parameters on vibration response, we compute the frequency spectra of vibration signals obtained by two types of dynamic parameters and separately compare them with the frequency spectrum of the measured signal. The comparative results in the CWRU experiment are shown in Figs. 8(a) and (b). The frequency spectrum obtained by the proposed inverse PINN is close to that of the measured signal, and the main frequency components of the frequency spectrum based on the empirical parameters greatly deviate from those of a real signal. The comparative results in the XJTU experiment are drawn in Figs. 9(a) and (b). A similar conclusion is obtained.

Furthermore, the time-frequency spectra of the simulated and measured signals in the two experiments are calculated by short-time Fourier transform. The calculation results for the CWRU experiment are illustrated in Figs. 10(a)-(c), and the calculation results for the XJTU experiment are displayed in Figs. 10(d)-(f). The simulated

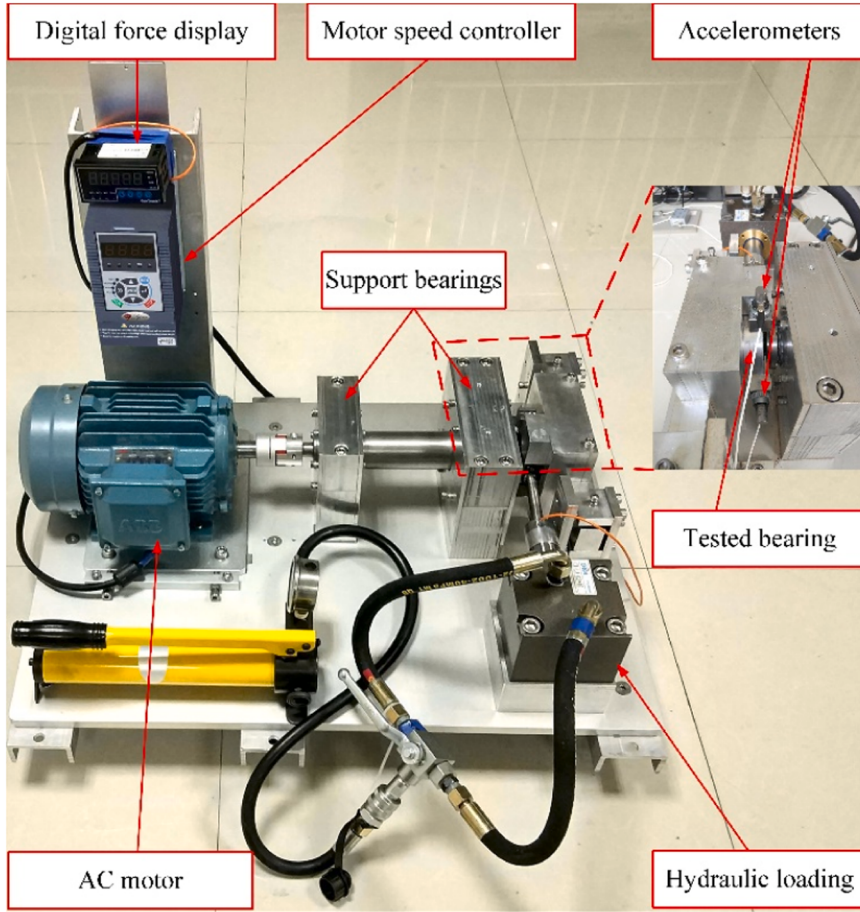


Fig. 6. Faulty rolling bearing test rig used by XJTU.

**Table 3**  
Bearing parameters from XJTU.

Parameter	Value
Number of balls ( $n$ )	8
Roller diameter ( $d/\text{mm}$ )	7.92
Pitch diameter ( $d_m/\text{mm}$ )	34.55
Inner race diameter ( $d_i/\text{mm}$ )	29.30
Outer race diameter ( $d_o/\text{mm}$ )	39.80
Initial contact angle ( $\alpha/^\circ$ )	0

**Table 4**  
Dynamic parameters obtained by inverse PINN and expertise in two experiments.

Experiment	Type of parameters	Stiffness $K$ ( $\text{N}/\text{m}$ )	Damping ratio $c$ ( $(\text{N}\cdot\text{s})/\text{m}$ )
CWRU	Optimized parameters obtained by the inverse PINN	$1.09 \times 10^9$	155
	Empirical parameters	$1.3 \times 10^{10}$	300
XJTU	Optimized parameters obtained by the inverse PINN	$1.39 \times 10^8$	162
	Empirical parameters	$4.34 \times 10^9$	200

time–frequency spectrum based on the parameters optimized by the inverse PINN is similar to the real time–frequency spectrum of the faulty bearing. Notably, the frequency range where the energy is concentrated in Fig. 10(b) is consistent with that in Fig. 10(c), indicating that the inverse PINN can accurately identify the unknown dynamic parameters of a bearing, that it, it allows mapping from an actual physical space to a

virtual space in a digital twin model.

According to the frequency spectrum and time–frequency spectrum of a vibration signal, the natural frequency of a bearing can be estimated by the maximum peak. To show the advantage of the proposed parameter optimization approach over other methods, the errors and error rates of natural frequencies estimated by the inverse PINN and expertise are computed. The results in the two experiments are shown in Table 5. The natural frequency estimated by the proposed inverse PINN is highly precise, implying that the proposed inverse PINN can solve dynamic parameters and increase the accuracy of a simulation model.

Next, to quantify the difference between the simulation data and the measured data, we employ three indexes: percent root mean square difference (PRD), RMSE, and max mean discrepancy (MMD).

The commonly used PRD is defined as

$$PRD = \sqrt{\frac{\sum_{n=1}^N (x(n) - \hat{x}(n))^2}{\sum_{n=1}^N (x(n))^2}} \times 100, \quad (12)$$

where  $x$  denotes the real signal,  $\hat{x}$  represents the simulation signal, and  $N$  denotes the data length.

The RMSE can reflect the stability between two signals and is written as

$$RMSE = \sqrt{\frac{\sum_{n=1}^N (x(n) - \hat{x}(n))^2}{N}}, \quad (13)$$

The MMD is generally utilized for measuring the distance between two distributions (or signals) and evaluating their similarity. The level of

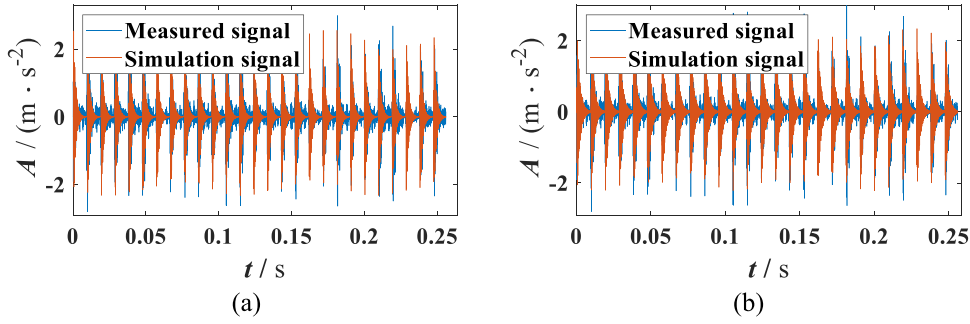


**Fig. 7.** Comparison of the simulated and measured signals in the CWRU experiment: (a) simulation result obtained by the optimized parameters; (b) simulation result obtained by the empirical parameters.

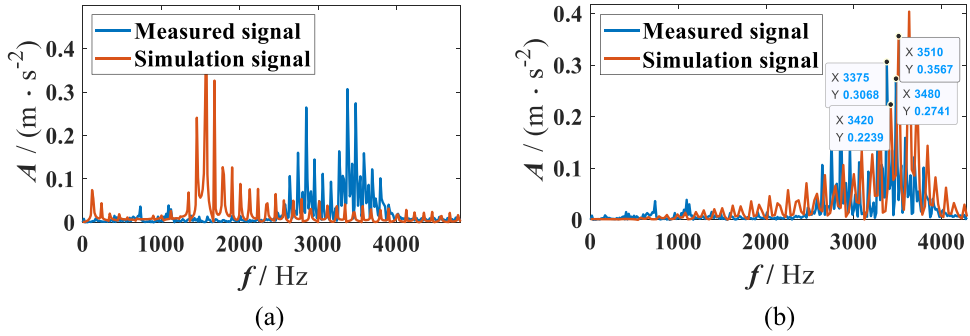


**Fig. 8.** Comparison of the simulated and experimental frequency spectra in the CWRU experiment: (a) simulation result based on the empirical parameters; (b) simulation result based on the parameters optimized by the inverse PINN.

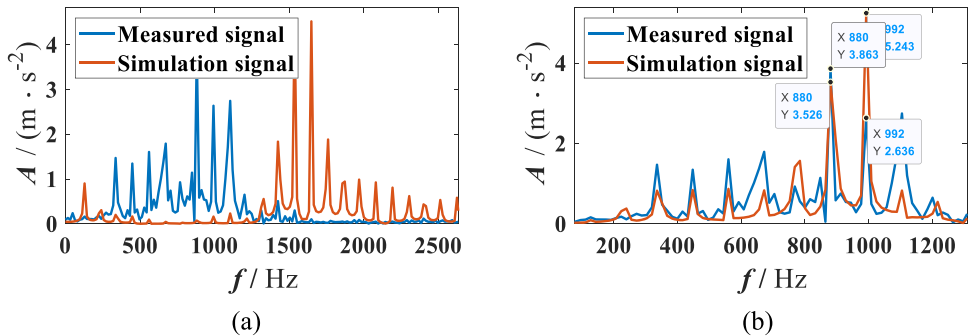


**Fig. 9.** Comparison of the simulated and experimental frequency spectra in the XJTU experiment: (a) simulation result based on the empirical parameters; (b) simulation result based on the parameters optimized by the inverse PINN.

similarity between two signals increases with decreasing MMD value. The MMD is given by

$$MMD[F, p, q] = \sup_{f \in F} (E_{x \sim p}[f(x)] - E_{\hat{x} \sim q}[f(\hat{x})]) \quad (14)$$

where  $p$  and  $q$  are the distributions of  $x$  and  $\hat{x}$ , respectively;  $F$  denotes the set of mapping functions; and  $f$  is generally taken as a Gaussian kernel function.

The simulation signals obtained by the optimized and empirical parameters are quantitatively evaluated from the time and frequency domains. First, the time-domain evaluation of simulation data is performed. The results of two experiments are shown in Table 6. Second, the frequency spectra of simulation data are computed by Fourier transform, and frequency-domain evaluation is executed. The results of the two experiments are listed in Table 7. The time-domain and frequency-domain simulation signals obtained by the inverse PINN have minimum PRDs, RMSEs, and MMDs in the two experiments. The time-domain MMD obtained by the inverse PINN in the CWRU experiment

is much smaller than that obtained by experience, and the frequency-domain PRD and RMSE obtained by the inverse PINN in the XJTU experiment are much smaller than those obtained by experience. Therefore, the dynamic parameters identified by the proposed inverse PINN can make the simulated vibration signals closer to the actual vibration signal in a physical space.

#### 4.4. Example of data generation

After the dynamic parameters of bearing are identified by the inverse PINN, the vibration response of faulty bearing under any working condition can be simulated by the developed digital twin-based fault data-generation method. The bearing fault data-generation in the XJTU experiment is taken as an example. The bearing vibration signal acquired under a rotational frequency of 35 Hz and load of 12 kN is employed for the identification of dynamic parameters with the inverse PINN. Bearing vibration data with outer ring fault (ORF) under a rotational frequency of 40 Hz and load of 10 kN are generated with the

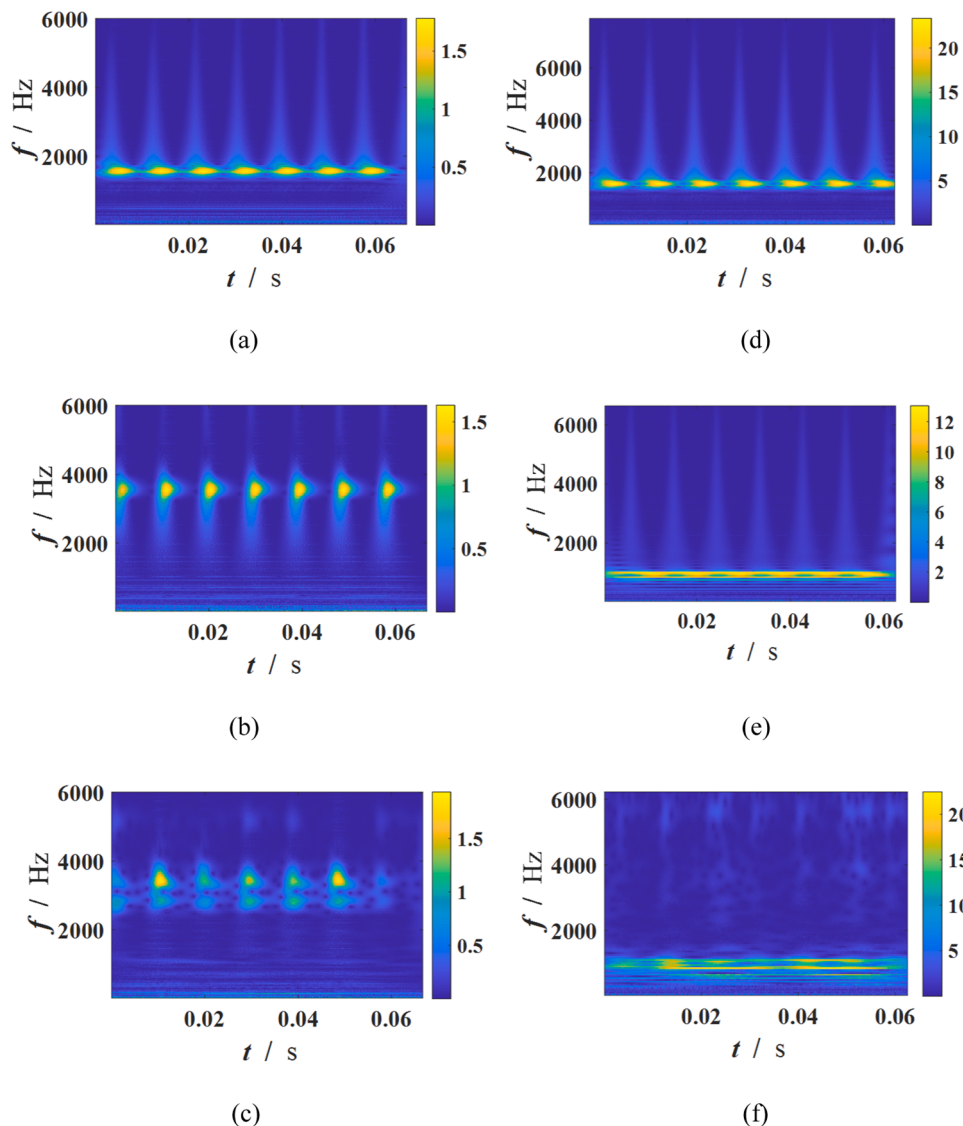


**Fig. 10.** Comparison of the simulated and experimental time–frequency spectra: (a) CWRU simulation result based on the empirical parameters; (b) CWRU simulation result based on the parameters optimized by the inverse PINN; (c) CWRU real result; (d) XJTU simulation result based on the empirical parameters; (e) XJTU simulation result based on the parameters optimized by the inverse PINN; (f) XJTU real result.

**Table 5**  
Error rate of signal spectrum when different parameters are used.

Dataset	Source of parameters	The deviation rate of natural frequency	The deviation rate of natural frequency
CWRU	Optimized parameters obtained by the inverse PINN	1.33 %	0.86 %
	Empirical parameters	53.33 %	51.72 %
XJTU	Optimized parameters obtained by the inverse PINN	0 %	0 %
	Empirical parameters	74.55 %	66.13 %

obtained dynamic parameters and bearing fault dynamic model. The frequency spectra of the produced and measured signals are computed (Fig. 11). The two frequency spectra have similar characteristic spectral lines, that is, the main characteristic frequency components in the bearing vibration signal are effectively simulated and produced.

In addition, the frequencies at the maximum and submaximum

**Table 6**  
Evaluation results of time-domain signals for different parameters.

Dataset	Type of parameters	PRD	RMSE	MMD
CWRU	Optimized parameters obtained by the inverse PINN	15.6680	0.6630	0.0012
	Empirical parameters	18.0585	0.7987	0.0024
XJTU	Optimized parameters obtained by the inverse PINN	11.2012	6.2905	0.1945
	Empirical parameters	14.0877	7.9115	0.3035

**Table 7**  
Evaluation results of frequency spectra for different parameters.

Dataset	Type of parameters	PRD	RMSE	MMD
CWRU	Optimized parameters obtained by the inverse PINN	8.3618	0.0514	0.1810
	Empirical parameters	13.2925	0.0534	0.2647
XJTU	Optimized parameters obtained by the inverse PINN	6.8781	0.1932	1.1014
	Empirical parameters	13.1540	0.3694	1.3907

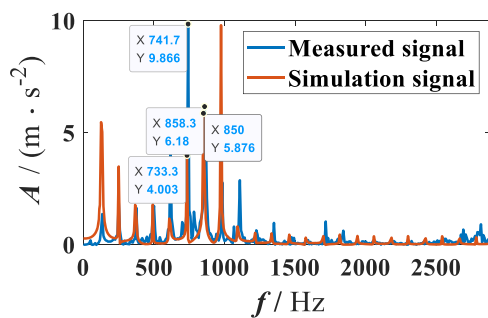


**Fig. 11.** Frequency spectra of simulated and measured bearing vibration signals with outer ring fault sample at a rotational frequency of 40 Hz and load of 10 kN.

**Table 8**  
Evaluation results of the generated bearing vibration signal.

Error rate of frequency at the maximum spectral peak	Error rate of frequency at the submaximum spectral peak	PRD	RMSE	MMD
1.07 %	0.93 %	12.2763	8.6220	0.1471

**Table 9**  
Structure parameters of diagnostic network.

Type of layer	Core size/stride	Number of cores	Output size
Conv 1	4 × 4/2	64	(50, 50, 64)
Conv 1	4 × 4/2	128	(25, 25, 128)
Conv 2	4 × 4/2	256	(13, 13, 256)
Conv 3	4 × 4/1	3	(13, 13, 3)
GlobalMaxPool	/	/	3

spectral peaks are selected for the computation of error rates (Table 8). Meantime, the PRD, RMSE and MMD of the simulated time-domain signal are calculated and shown in Table 8. The simulation signal has small errors in characteristic frequencies, hence ensuring the quality of generated data.

## 5. Application into bearing fault diagnosis

### 5.1. Case I: few samples for a working condition

To examine the value of the proposed data augmentation approach in fault bearing diagnosis, we implement the cross-working-condition bearing fault diagnosis with the imbalanced samples. First, the bearing fault vibration data from the XJTU experiment is employed for the fault diagnosis experiment. For 1800 healthy samples, 1800 inner ring fault (IRF) samples and 1350 ORF samples are used for training and testing. When the rotational frequency is 37.5 or 35 Hz, 600 healthy, 600 IRF,

**Table 11**

XJTU experiment results of three trained CNNs in the case of using 50 outer ring fault samples.

Training dataset	Real label	Predicted label			Average accuracy
		Healthy	IRF	ORF	
Real dataset	Healthy	1.00	0	0	0.8900
	IRF	0	1.00	0	
	ORF	0	0.33	0.67	
Augmented dataset by inverse PINN	Healthy	1.00	0	0	0.9800
	IRF	0	1.00	0	
	ORF	0	0.06	0.94	
Augmented dataset by expertise	Healthy	1.00	0	0	0.9100
	IRF	0	1.00	0	
	ORF	0	0.27	0.73	

and 600 ORF samples are selected under each working condition. When the rotational frequency is 40 Hz, 600 healthy, 600 IRF, and 150 ORF samples are utilized. Sample imbalance for the ORF is observed.

To address this problem, the proposed digital twin-based fault data-generation method is used to augment fault samples at a rotational frequency of 40 Hz. By setting different fault sizes in a small range and adding Gaussian random noises, 450 ORF samples at a rotational frequency of 40 Hz are generated to increase data diversity. To demonstrate the superiority of the dynamic parameters identified by the inverse PINN over those identified through other methods, ORF samples are generated by the bearing fault dynamic model with empirically dynamic parameters. Given that the diagnostic model in actual engineering requires low computational complexity and fast calculation speed, the number of samples is small. Thus, we design a simple CNN for bearing fault classification. The specific structure parameters of the diagnostic model are listed in Table 9. Two training datasets are built from the augmented samples based on two methods (Table 10). Moreover, the training dataset is built using only real samples (Table 10). Other real bearing vibration samples will be used for testing, that is, 100 samples under each health status are used for testing.

After the diagnostic networks are trained with the three training datasets, diagnostic performance is evaluated with the test dataset. The comparative results are presented in Table 11. The diagnostic accuracy of the ORF is low because real training samples are rare at a rotational frequency of 40 Hz. By introducing the generated ORF samples, the diagnostic accuracy of the ORF increases, whereas the classification ability of the other two health states shows no change. Compared with the traditional data-generation method based on the dynamic model with expertise, the developed data-generation method based on the inverse PINN can better improve the diagnostic accuracy of ORF. The average diagnostic precision obtained by the augmented dataset based on the inverse PINN is 98 %, which is 9 % higher than that obtained by the real dataset and 7 % higher than that obtained by the augmented dataset based on the traditional dynamic model. Hence, the proposed data-generation method is more effective than traditional methods in

**Table 10**  
Details of three training datasets with 50 outer ring fault samples for the rotational frequency of 40 Hz.

Datasets	Rotational frequency (Hz)	Load (kN)	Healthy bearing	IRF bearing	ORF bearing	Augmented fault samples
Real dataset	35	12	500	500	500	0
	37.5	11	500	500	500	0
	40	10	500	500	50	0
Augmented dataset by inverse PINN	35	12	500	500	500	0
	37.5	11	500	500	500	0
	40	10	500	500	50	450
Augmented dataset by expertise	35	12	500	500	500	0
	37.5	11	500	500	500	0
	40	10	500	500	50	450

**Table 12**

CWRU experiment results of three trained CNNs when 50 outer ring fault samples are used.

Training dataset	Real label	Predicted label			Average accuracy
		Healthy	IRF	ORF	
Real dataset	Healthy	1.00	0	0	0.9467
	IRF	0	1.00	0	
	ORF	0	0.16	0.84	
Augmented dataset by inverse PINN	Healthy	1.00	0	0	<b>1.0000</b>
	IRF	0	1.00	0	
	ORF	0	0	1.00	
Augmented dataset by expertise	Healthy	1.00	0	0	0.9667
	IRF	0	1.00	0	
	ORF	0	0.10	0.90	

**Table 13**

XJTU experiment results of different methods when 50 outer ring fault samples are used.

Method	Real label	Predicted label			Average accuracy
		Healthy	IRF	ORF	
CycleGAN	Healthy	1.00	0	0	0.9600
	IRF	0	1.00	0	
	ORF	0	0.12	0.88	
Phenomenological model	Healthy	1.00	0	0	0.9567
	IRF	0	1.00	0	
	ORF	0	0.13	0.87	
Zero-shot learning	Healthy	1.00	0	0	0.9267
	IRF	0.02	0.82	0.16	
	ORF	0.01	0.03	0.96	
WDCNN	Healthy	1.00	0	0	0.9367
	IRF	0.17	0.83	0	
	ORF	0.02	0	0.98	
Proposed method	Healthy	1.00	0	0	<b>0.9800</b>
	IRF	0	1.00	0	
	ORF	0	0.06	0.94	

**Table 14**

CWRU experiment results of different methods when 50 outer ring fault samples are used.

Method	Real label	Predicted label			Average accuracy
		Healthy	IRF	ORF	
CycleGAN	Healthy	1.00	0	0	0.9700
	IRF	0	1.00	0	
	ORF	0	0.09	0.91	
Phenomenological model	Healthy	1.00	0	0	0.9667
	IRF	0	1.00	0	
	ORF	0	0.10	0.90	
Zero-shot learning	Healthy	1.00	0	0	0.9633
	IRF	0.03	0.97	0	
	ORF	0.05	0.03	0.92	
WDCNN	Healthy	0.99	0.01	0	0.9367
	IRF	0.10	0.90	0	
	ORF	0.07	0.01	0.92	
Proposed method	Healthy	1.00	0	0	<b>1.0000</b>
	IRF	0	1.00	0	
	ORF	0	0	1.00	

improving the accuracy of bearing fault diagnosis for imbalanced samples.

Next, the bearing fault vibration data from CWRU are used for the fault diagnosis experiment. However, only 50 actual ORF samples for the 3 hp load are used. A similar procedure is executed, and three training datasets are built. The test accuracy of the CNNs trained by

**Table 15**

XJTU experiment results of three trained CNNs in the case of using 20 outer ring fault samples.

Training dataset	Real label	Predicted label			Average accuracy
		Healthy	IRF	ORF	
Real dataset	Healthy	1	0	0	0.8867
	IRF	0	1	0	
	ORF	0	0.34	0.66	
Augmented dataset by inverse PINN	Healthy	1	0	0	<b>0.9733</b>
	IRF	0	1	0	
	ORF	0	0.08	0.92	
Augmented dataset by expertise	Healthy	1	0	0	0.9000
	IRF	0	1	0	
	ORF	0	0.30	0.70	

**Table 16**

XJTU experiment results of different methods in the case of using 20 outer ring fault samples.

Method	Real label	Predicted label			Average accuracy
		Healthy	IRF	ORF	
CycleGAN	Healthy	1	0	0	0.9567
	IRF	0	1	0	
	ORF	0	0.13	0.87	
Phenomenological model	Healthy	1	0	0	0.9467
	IRF	0	1	0	
	ORF	0	0.16	0.84	
Zero-shot learning	Healthy	1	0	0	0.9167
	IRF	0.04	0.84	0.12	
	ORF	0.07	0.02	0.91	
WDCNN	Healthy	1	0	0	0.9200
	IRF	0.17	0.81	0	
	ORF	0.02	0	0.95	
Proposed method	Healthy	1	0	0	<b>0.9733</b>
	IRF	0	1	0	
	ORF	0	0.08	0.92	

them is shown in the Table 12. The comparative results show that the proposed approach outperforms the traditional data-generation method and increases the accuracy of imbalanced bearing fault diagnosis.

Additionally, to further check the effectiveness and merit of the proposed approach in solving the issue of imbalanced samples, we compare it with other advanced data-generation methods, such as the phenomenological model [29] and CycleGAN [18]. SOTA intelligent diagnosis methods for imbalanced fault diagnosis, including zero sample learning [30] and WDCNN [31], whose network model structures are basically the same as those in these references, are used for comparison. The methods are applied to the fault classification of the same test dataset, and their diagnostic accuracy for different health states is computed. The comparative results in the XJTU and CWRU experiments are shown in Tables 13 and 14, respectively. The proposed approach has the highest average diagnostic precision in both experiments among all the used methods. Especially in the XJTU experiment, it has the highest accuracy for each health status. The above results verify that the proposed approach indeed solves the issue of imbalanced samples and is superior to other typical and SOTA methods.

Finally, we use the XJTU bearing data to investigate the effect of number of imbalanced samples on fault diagnosis accuracy. In this experiment, we use 20 actual ORF samples at a rotational frequency of 40 Hz in the training set. The traditional data-generation method, advanced data-generation methods, and SOTA intelligent imbalanced fault diagnosis methods are used for comparison. The comparative results between the proposed method and the traditional data-generation method are shown in Table 15, and those between the proposed and

**Table 17**

Details of the three training datasets in case II.

Datasets	Rotational frequency (Hz)	Load (kN)	Healthy bearing	IRF bearing	ORF bearing	Augmented fault samples
Real dataset	35	12	500	500	500	0
	37.5	11	500	500	500	0
	40	10	500	500	0	0
Augmented dataset by inverse PINN	35	12	500	500	500	0
	37.5	11	500	500	500	0
	40	10	500	500	0	500
Augmented dataset by expertise	35	12	500	500	500	0
	37.5	11	500	500	500	0
	40	10	500	500	0	500

**Table 18**

XJTU experiment results of three trained CNNs in case II.

Training dataset	Real label	Predicted label			Average accuracy
		Healthy	IRF	ORF	
Real dataset	Healthy	1.00	0	0	0.8700
	IRF	0	1.00	0	
	ORF	0	0.39	0.61	
Augmented dataset by inverse PINN	Healthy	1.00	0	0	<b>0.9400</b>
	IRF	0	1.00	0	
	ORF	0	0.18	0.82	
Augmented dataset by expertise	Healthy	1.00	0	0	0.9033
	IRF	0	1.00	0	
	ORF	0	0.29	0.71	

**Table 19**

CWRU experiment results of three trained CNNs in case II.

Training dataset	Real label	Predicted label			Average accuracy
		Healthy	IRF	ORF	
Real dataset	Healthy	1.00	0	0	0.9100
	IRF	0	1.00	0	
	ORF	0	0.27	0.73	
Augmented dataset by inverse PINN	Healthy	1.00	0	0	<b>0.9500</b>
	IRF	0	1.00	0	
	ORF	0	0.15	0.85	
Augmented dataset by expertise	Healthy	1.00	0	0	0.9367
	IRF	0	1.00	0	
	ORF	0	0.19	0.81	

advanced methods are shown in [Table 16](#). From these results, we can see that the proposed method can be effectively applied to the bearing fault diagnosis with varying number of imbalanced samples (i.e., different balance rates).

### 5.2. Case II: missing data for a working condition

When no bearing fault data are obtained under a certain working condition, cross-domain fault diagnosis is difficult to implement. The proposed method and the traditional data-generation method are respectively applied to augment the bearing fault samples under this working condition. Then, two training datasets are constructed. The training dataset is built using only the real samples. The details of the three training datasets are shown in [Table 17](#).

Three training datasets are used for training networks, and their capabilities are validated using the test dataset. The comparative results are shown in [Table 18](#). The diagnostic accuracy of the ORF is low because the real training samples at a rotational frequency of 40 Hz are missing. After the generated ORF samples are added, the diagnostic accuracy of the ORF improves, and the average accuracy obtained by the

**Table 20**

XJTU experiment results of different methods in case II.

Method	Real label	Predicted label			Average accuracy
		Healthy	IRF	ORF	
CycleGAN	Healthy	1.00	0	0	0.9200
	IRF	0	1.00	0	
	ORF	0	0.24	0.76	
Phenomenological model	Healthy	1.00	0	0	0.9267
	IRF	0	1.00	0	
	ORF	0	0.22	0.78	
Zero-shot learning	Healthy	1.00	0	0	0.8733
	IRF	0	1.00	0	
	ORF	0.04	0.34	0.62	
WDCNN	Healthy	1.00	0	0	0.8700
	IRF	0.12	0.88	0	
	ORF	0	0.27	0.73	
Proposed method	Healthy	1.00	0	0	<b>0.9400</b>
	IRF	0	1.00	0	
	ORF	0	0.18	0.82	

**Table 21**

CWRU experiment results of different methods in the case II.

Method	Real label	Predicted label			Average accuracy
		Healthy	IRF	ORF	
CycleGAN	Healthy	1.00	0	0	0.9200
	IRF	0	1.00	0	
	ORF	0	0.24	0.76	
Phenomenological model	Healthy	1.00	0	0	0.9067
	IRF	0	1.00	0	
	ORF	0	0.28	0.72	
Zero-shot learning	Healthy	1.00	0	0	0.9333
	IRF	0	0.93	0	
	ORF	0.05	0.08	0.87	
WDCNN	Healthy	1.00	0	0	0.9133
	IRF	0.01	0.99	0	
	ORF	0	0.25	0.75	
Proposed method	Healthy	1.00	0	0	<b>0.9500</b>
	IRF	0	1.00	0	
	ORF	0	0.15	0.85	

augmented dataset based on the inverse PINN is up to 94 %. Furthermore, the proposed method is better in increasing the diagnostic accuracy of the ORF than the traditional data-generation method.

The bearing fault vibration data from CWRU is used for the fault diagnosis experiment. The actual ORF samples acquired under a load of 3 hp are not used. The traditional data-generation method based on the dynamic model with expertise and the proposed method are applied to augment the fault samples at this load. Three datasets are built for the training of the diagnostic CNNs. The test results are listed in [Table 19](#). The proposed approach is superior to the traditional data-generation method, and the fault diagnosis accuracy for the imbalanced samples is effectively improved ([Tables 18 and 19](#)).

Using the XJTU and CWRU datasets, the proposed approach is compared with the foregoing methods, including the phenomenological model, CycleGAN, zero sample learning, and WDCNN. The experimental results of the XJTU and CWRU datasets are illustrated in Tables 20 and 21, respectively. The proposed approach achieves a higher diagnostic accuracy than the other SOTA methods. Thus, the superiority of the proposed digital twin-based method for the imbalanced bearing fault diagnosis to other methods is validated.

## 6. Conclusions

A bearing data-generation approach for enhancing the capability of cross-working-condition bearing fault diagnosis for imbalanced samples is investigated. To accurately identify the dynamic parameters of bearing, we establish a novel inverse PINN by incorporating the bearing dynamics model into a neural network. The principle of this network is contrary to a traditional PINN. In the inverse PINN, boundary loss and truth loss are built to accelerate network convergence and used in the evaluation of difference between the simulated and real frequency-domain data. With the inverse PINN, fault bearing dynamic model, and acquired actual data, a digital twin-based fault data-generation approach is proposed to produce bearing fault signals that supplement samples under a specific working condition. Then, they are used to train the fault diagnosis network. The experimental results demonstrate that the proposed method can effectively overcome the problem of sample balance in bearing fault diagnosis and is superior to the SOTA data-generation and imbalanced fault diagnosis methods. In the future, we will identify model parameters from measured signals with strong background noise and further enhance the quality and diversity of generated data.

## Declaration of competing interest

The authors declare that they have no known competing financial interests or personal relationships that could have appeared to influence the work reported in this paper.

## Acknowledgments

The work described in this paper was supported by the National Natural Science Foundation of China (no. 52175075).

## References

- [1] X. Jiang, J. Wang, C. Shen, J. Shi, W. Huang, Z. Zhu, Q. Wang, An adaptive and efficient variational mode decomposition and its application for bearing fault diagnosis, *Struct. Health Monitor.- An Internat. J.* 20 (5) (2021) 2708–2725.
- [2] Q. Qian, Y. Wang, T. Zhang, Y. Qin, Maximum mean square discrepancy: a new discrepancy representation metric for mechanical fault transfer diagnosis, *Knowl. Based. Syst.* 276 (2023) 110748.
- [3] K. Su, J. Liu, H. Xiong, Hierarchical diagnosis of bearing faults using branch convolutional neural network considering noise interference and variable working conditions, *Knowl. Based. Syst.* 230 (2021) 107386.
- [4] X. Wang, Y. Qin, Y. Wang, S. Xiang, H.J.N. Chen, ReLTanh: an activation function with vanishing gradient resistance for SAE-based DNNs and its application to rotating machinery fault diagnosis, *Neurocomputing*, 363 (2019) 88–98.
- [5] R. Wang, W.G. Huang, M.K. Shi, J. Wang, C.Q. Shen, Z.K. Zhu, Federated adversarial domain generalization network: a novel machinery fault diagnosis method with data privacy, *Knowl. Based. Syst.* 256 (2022) 109880.
- [6] M.H. Zhao, X.Y. Fu, Y.J. Zhang, L.H. Meng, B.P. Tang, Highly imbalanced fault diagnosis of mechanical systems based on wavelet packet distortion and convolutional neural networks, *Adv. Eng. Informat.* 51 (2022) 101535.
- [7] Q. Xu, S. Lu, W. Jia, C. Jiang, Imbalanced fault diagnosis of rotating machinery via multi-domain feature extraction and cost-sensitive learning, *J. Intell. Manuf.* 31 (2020) 1467–1481.
- [8] D. Li, S. Liu, F. Gao, X. Sun, Continual learning classification method and its application to equipment fault diagnosis, *Appl. Intelligence* 52 (2022) 858–874.
- [9] X.Y. Wang, Z.Y. Chu, B.K. Han, J.R. Wang, G.W. Zhang, X.X. Jiang, A novel data augmentation method for intelligent fault diagnosis under speed fluctuation condition, *IEEE Access*, 8 (2020) 143383–143396.
- [10] Z. An, X. Jiang, R. Yang, H. Zhang, J. Liu, C. Shen, Actively imaginative data augmentation for machinery diagnosis under large speed fluctuation conditions, *IEEE Trans. Industr. Inform.* (2022).
- [11] Z. Pei, H. Jiang, X. Li, J. Zhang, S. Liu, Data augmentation for rolling bearing fault diagnosis using an enhanced few-shot Wasserstein auto-encoder with meta-learning, *Measure. Sci. Techn.* 32 (2021) 084007.
- [12] Y.M. Xiao, H.D. Shao, S.Y. Han, Z.Q. Huo, J.F. Wan, Novel joint transfer network for unsupervised bearing fault diagnosis from simulation domain to experimental domain, *IEEE-ASME Trans. Mech.* 27 (2022) 5254–5263.
- [13] Y. Qin, Q. Li, S. Wang, P. Cao, Dynamics modeling of faulty planetary gearboxes by time-varying mesh stiffness excitation of spherical overlapping pittings, *Mech. Syst. Signal Process.* 210 (2024) 111162.
- [14] C. Liu, A. Ricardo Mauricio, J. Qi, D. Peng, K. Gryllias, Domain adaptation digital twin for rolling element bearing prognostics, *Online Proceed. PHM 2020* (2020) 1–10.
- [15] X. Liu, H. Huang, J. Xiang, A personalized diagnosis method to detect faults in a bearing based on acceleration sensors and an FEM simulation driving support vector machine, *Sensors* 20 (2020) 420.
- [16] F. Piltan, J.M. Kim, Crack size identification for bearings using an adaptive digital twin, *Sensors* 21 (2021).
- [17] Y. Qin, X.G. Wu, J. Luo, Data-model combined driven digital twin of life-cycle rolling bearing, *IEEE Trans. Industr. Inform.* 18 (2022) 1530–1540.
- [18] J.Y. Zhu, T. Park, P. Isola, A.A. Efros, Unpaired image-to-image translation using cycle-consistent adversarial networks, in: 16th IEEE International Conference on Computer Vision (ICCV), Venice, ITALY, 2017, pp. 2242–2251.
- [19] X. Chen, M. Ma, Z. Zhao, Z. Zhai, Z. Mao, Physics-informed deep neural network for bearing prognosis with multisensory signals, *J. Dynamics, Monitor. Diagnostics* (2022) 200–207.
- [20] Y.A. Yucesan, F.A. Viana, A physics-informed neural network for wind turbine main bearing fatigue, *Internat. J. Prognostics Health Manage.* 11 (2020).
- [21] J. Ling, A. Kurzawski, J. Tembleton, Reynolds averaged turbulence modelling using deep neural networks with embedded invariance, *J. Fluid. Mech.* 807 (2016) 155–166.
- [22] Z.P. Mao, A.D. Jagtap, G.E. Karniadakis, Physics-informed neural networks for high-speed flows, *Comput. Methods Appl. Mech. Eng.* 360 (2020).
- [23] G.E. Karniadakis, I.G. Kevrekidis, L. Lu, P. Perdikaris, S. Wang, L. Yang, Physics-informed machine learning, *Nat. Rev. Phys.* 3 (2021) 422–440.
- [24] M.J.W.P. Grieves, Digital twin: manufacturing excellence through virtual factory replication, *White Paper* 1 (2014) 1–7.
- [25] E. Glæssgen, D. Stargel, The digital twin paradigm for future NASA and US Air Force vehicles, in: 53rd AIAA/ASME/ASCE/AHS/ASC structures, structural dynamics and materials conference 20th AIAA/ASME/AHS adaptive structures conference 14th AIAA, 2012, p. 1818.
- [26] B. Deon, K.P. Cotta, N. Padoin, Digital twin and machine learning for decision support in thermal power plant with combustion engines, *Knowl. Based. Syst.* 253 (2022) 107386.
- [27] C. Li, Y. Qin, Y. Wang, H. Chen, Vibration analysis of deep groove ball bearings with local defect using a new displacement excitation function, *J. Tribol.* 142 (2020) 121202.
- [28] B. Wang, Y. Lei, N. Li, N. Li, A hybrid prognostics approach for estimating remaining useful life of rolling element bearings, *IEEE Trans. Reliab.* 69 (2018) 401–412.
- [29] C. Liu, K. Gryllias, Simulation-driven domain adaptation for rolling element bearing fault diagnosis, *IEEE Trans. Industr. Inform.* 18 (2021) 5760–5770.
- [30] L.J. Feng, C.H. Zhao, Fault description based attribute transfer for zero-sample industrial fault diagnosis, *IEEE Trans. Industr. Inform.* 17 (2021) 1852–1862.
- [31] W. Zhang, G.L. Peng, C.H. Li, Y.H. Chen, Z.J. Zhang, A new deep learning model for fault diagnosis with good anti-noise and domain adaptation ability on raw vibration signals, *Sensors* 17 (2) (2017) 425.